

# Joint Estimation of Activity and Attenuation in Whole-Body TOF PET/MRI Using Constrained Gaussian Mixture Models

Abolfazl Mehranian, *Student Member, IEEE*, and Habib Zaidi\*, *Senior Member, IEEE*

**Abstract**—It has recently been shown that the attenuation map can be estimated from time-of-flight (TOF) PET emission data using joint maximum likelihood reconstruction of attenuation and activity (MLAA). In this work, we propose a novel MRI-guided MLAA algorithm for emission-based attenuation correction in whole-body PET/MR imaging. The algorithm imposes MR spatial and CT statistical constraints on the MLAA estimation of attenuation maps using a constrained Gaussian mixture model (GMM) and a Markov random field smoothness prior. Dixon water and fat MR images were segmented into outside air, lung, fat and soft-tissue classes and an MR low-intensity (unknown) class corresponding to air cavities, cortical bone and susceptibility artifacts. The attenuation coefficients over the unknown class were estimated using a mixture of four Gaussians, and those over the known tissue classes using unimodal Gaussians, parameterized over a patient population. To eliminate misclassification of spongy bones with surrounding tissues, and thus include them in the unknown class, we heuristically suppressed fat in water images and also used a co-registered bone probability map. The proposed MLAA-GMM algorithm was compared with the MLAA algorithms proposed by Rezaei *et al.* and Salomon *et al.* using simulation and clinical studies with two different tracer distributions. The results showed that our proposed algorithm outperforms its counterparts in suppressing the cross-talk and scaling problems of activity and attenuation and thus produces PET images of improved quantitative accuracy. It can be concluded that the proposed algorithm effectively exploits the MR information and can pave the way toward accurate emission-based attenuation correction in TOF PET/MRI.

**Index Terms**—Attenuation correction, Gaussian mixture models, MLAA, reconstruction, TOF PET/MRI.

## I. INTRODUCTION

**H**YBRID PET/MR systems have recently been introduced in clinical practice as a new diagnostic imaging modality offering the capability to combine molecular and morpholog-

ical assessment of a variety of physiopathological conditions [1]. Thanks to advances in radiation detectors and PET instrumentation, PET/MR has now adequately addressed the mutual compatibility challenge between PET and MRI components. However, MRI-based attenuation correction (MRAC) remains as another major challenge owing to the lack of bone signal in conventional MR sequences and a unique global mapping between MR image intensities and corresponding attenuation coefficients [2], [3].

Overall, MRAC methods can be categorized into three classes: i) segmentation-based approaches, in which MR images are segmented into different tissue classes followed by assignment of predefined attenuation coefficients to each class [4], [5], ii) atlas registration-based approaches, in which a co-registered MR-CT atlas dataset is used to derive a pseudo CT image from the patient's MR image or to learn a mapping function that predicts the pseudo CT [6]–[9] and iii) emission-based approaches in which the attenuation map is estimated from PET emission data. Segmentation-based approaches usually do not take into account the presence of bones and the inter/intra-patient variability of attenuation coefficients, especially in the lungs. On the other hand, atlas registration based methods can solve the MRAC problem, particularly in brain imaging, provided that a perfect registration between the atlas and different patients can be achieved. However, a perfect whole-body registration is rarely possible owing to substantial anatomical differences between patients and their postures during scanning and current limitations of registration algorithms. Emission-based methods attempt to derive attenuation coefficients from emission data without using any estimate of the activity map, based on the consistency conditions of the attenuated Radon transform [10]–[12], or to simultaneously estimate activity and attenuation maps in a maximum likelihood (ML) framework [13]–[16]. The consistency conditions state that, in the absence of noise, a given emission data can only arise under certain attenuation conditions, or conversely for a given attenuation map, only certain emission data are possible. These conditions do not account for the statistical nature of emission data and generally cannot completely determine attenuation coefficients.

In the ML framework, the Poisson distribution of data is properly modeled and the joint likelihood is alternatively maximized with respect to activity and attenuation using a maximum likelihood reconstruction of attenuation and activity (MLAA) algorithm [14]. However, the estimated activity/attenuation pair often suffers from the so-called cross-talk artifacts, where the activity features propagate into the attenuation map and vice versa, reflecting the non-uniqueness of the solution. Therefore,

Manuscript received December 29, 2014; revised February 12, 2015; accepted February 28, 2015. Date of publication March 05, 2015; date of current version August 28, 2015. This work was supported by the Swiss National Science Foundation under Grant SNSF 31003A-149957 and the Indo-Swiss Joint Research Programme ISJRP 138866. *Asterisk indicates corresponding author.*

A. Mehranian is with Division of Nuclear Medicine and Molecular Imaging, Geneva University Hospital, CH-1211 Geneva, Switzerland (e-mail: abolfazl.mehranian@etu.unige.ch).

\*H. Zaidi is with Division of Nuclear Medicine and Molecular Imaging, Geneva University Hospital, CH-1211 Geneva, Switzerland, and also with Geneva Neuroscience Center, Geneva University, CH-1205 Geneva, Switzerland, and also with the Department of Nuclear Medicine and Molecular Imaging, University of Groningen, University Medical Center Groningen, 9700 RB Groningen, The Netherlands (e-mail: habib.zaidi@hcuuge.ch).

Color versions of one or more of the figures in this paper are available online at <http://ieeexplore.ieee.org>.

Digital Object Identifier 10.1109/TMI.2015.2409157

some constraints on attenuation and activity maps have to be defined in order to confine the solution space and to suppress cross-talks. The tissue preference priors [14], local smoothness priors [14], [17] and range constraints [18] were therefore used for attenuation estimation. With the advent of time-of-flight (TOF) PET/MR scanners [19], Salomon *et al.* [20], [21] imposed the inherent spatial constraint of TOF on activity estimation and the MR anatomical information on attenuation map estimation. Thereby, the noise and cross-talk artifacts were substantially reduced. In fact, it has been shown that TOF-PET image reconstruction can reduce the artifacts induced by attenuation correction errors [22], [23]. Using Fisher information-based analysis, Rezaei *et al.* [24] demonstrated that TOF can suppress cross-talks in the MLAA algorithm, however, they found that the reconstructed activity maps are globally scaled, while the attenuation maps show a position dependent scaling. Based on the range consistency conditions of the TOF attenuated Radon transform, Defrise *et al.* [25] also showed that attenuation correction factors can be determined from TOF-PET data up to a constant scaling factor. Overall, the performance of MLAA depends on (i) TOF timing resolution in order to suppress cross-dependencies between activity and attenuation maps, (ii) the count statistics of emission data for suppressing noisy estimations and (iii) the spatial distribution of the radiotracer in the body to support the estimation of attenuation map, which in turn depends on the injected radiotracer. Salomon *et al.* [21] proposed a region-wise estimation of attenuation coefficients over MRI-derived anatomical regions to reduce noise and crosstalk artifacts. However, in conventional MR sequences, bones cannot be discriminated from air and the images usually suffer from partial volume effect (PVE) leading to misclassification of bones with surrounding tissues, especially over the ribs and vertebrae. Moreover, depending on the number of regions, the region-wise estimation also might not allow for the local variability of attenuation values, especially in the lungs and vertebrae.

In this work, we aim at improving the performance of MLAA by exploiting segmented Dixon MR images and a co-registered bone probability map in order to define spatial and statistical constraints on the estimation of attenuation values using a constrained Gaussian mixture model (GMM) and Markov random field (MRF) smoothness prior. The proposed algorithm was compared with the original MLAA and Salomon's MLAA (MLAA-Salomon) algorithms.

## II. MATERIAL AND METHODS

### A. Objective Function

The measured TOF PET data,  $g_{it}$ , in LOR  $i$  and TOF bin  $t$  are best modeled as Poisson random variables with an expected value:

$$\bar{g}_{it} = n_i e^{-\sum_{k=1}^J l_{ik} \mu_k} \sum_{j=1}^J c_{ijt} \lambda_j + n_i \bar{s}_{it} + \bar{r}_{it} \quad (1)$$

where  $\lambda_j$  and  $\mu_k$  are activity and attenuation values at voxels  $j$  and  $k$ ,  $c_{ijt}$  is the geometric probability detection of annihilation events emitted from voxel  $j$  along LOR  $i$  in TOF bin  $t$ ,  $n_i$  is detector normalization factors,  $l_{ik}$  is the intersection length of LOR  $i$  with voxel  $k$ , and  $\bar{s}_{it}$  and  $\bar{r}_{it}$  are the expected values of scatter and random events, estimated by model-based methods

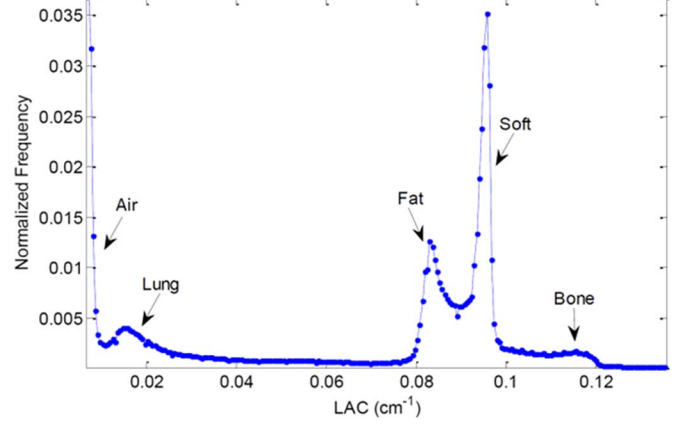


Fig. 1. The histogram of attenuation maps consists of a few distinct peaks corresponding to air, lung, fat, soft-tissue and bone.

and delayed coincidence window measurements, respectively. In the maximum *a posteriori* (MAP) framework, the unknowns  $\lambda$  and  $\mu$  are also modeled as random variables with prior densities, by which the solution space can be constrained. We exploited *a priori* knowledge about attenuation in the following joint MAP estimation:

$$(\hat{\lambda}, \hat{\mu}) = \arg \max_{\lambda \geq 0, \mu \geq 0} \left\{ \sum_{it} \{g_{it} \log(\bar{g}_{it}) - \bar{g}_{it}\} + \beta R_{MRF}(\mu) + \gamma R_{GMM}(\mu) \right\} \quad (2)$$

where  $R_{MRF}$  and  $R_{GMM}$  are MRF and Gaussian mixture priors to favor attenuation maps that are smooth, based on local intensity differences between adjacent voxels, and belong to a few distinct tissue classes according to the histogram of attenuation maps.  $\beta$  and  $\gamma$  are hyper-parameters, weighting the impact of the priors.  $R_{MRF}(\mu)$  is defined as:

$$R_{MRF}(\mu) = - \sum_{j=1}^J \sum_{k \in N_j} \omega_{jk} \psi(\mu_k - \mu_j), \quad \psi(t) = \frac{1}{2} t^2 \quad (3)$$

where  $N_j$  denotes a second-order neighborhood around the  $j$ th voxel with 26 nearest neighbors,  $\omega_{jk}$  is inversely proportional to the distance between voxel  $j$  and  $k$ , and  $\psi(t)$  is a quadratic potential function penalizing large differences between voxels. In  $R_{GMM}(\mu)$ , it is assumed that the attenuation coefficients are independent random variables with a density function that is a mixture of  $H$  known Gaussian density functions:

$$R_{GMM}(\mu) = \sum_{j=1}^J \log \left\{ \sum_{h=1}^H \pi_h \mathcal{N}(\mu_j | \bar{\mu}_h, \sigma_h) \right\} \\ \mathcal{N}(\mu_j | \bar{\mu}_h, \sigma_h) = \frac{1}{\sqrt{2\pi\sigma_h}} \exp \left( -\frac{1}{2} \left( \frac{\mu_j - \bar{\mu}_h}{\sigma_h} \right)^2 \right) \quad (4)$$

where  $\mathcal{N}(\mu_j | \bar{\mu}_h, \sigma_h)$  is the Gaussian density function associated with the  $h$ th component with mean  $\bar{\mu}_h$  and standard deviation  $\sigma_h$ ,  $\{\pi_h\}$  are mixture proportions that are assumed to be known and  $\sum_h \pi_h = 1$ . The mixture of Gaussians is used to reflect the fact that the histogram of the attenuation map consists of a few distinct peaks corresponding to air, lung, fat, soft-tissue and bone [26] (Fig. 1). In the proposed algorithm, we incorporate anatomical information derived from MR images into the GMM using a tissue prior map.

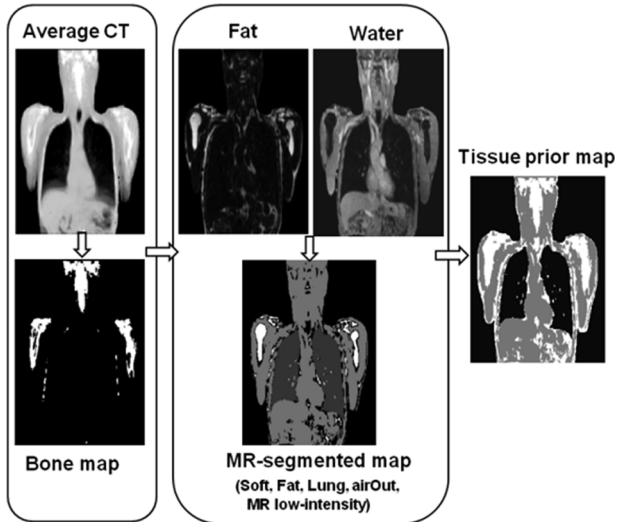


Fig. 2. Derivation of tissue prior map from Dixon MR and co-registered CT images.

### B. Tissue Prior Map and GMM Parameters

In this work, Dixon MR images, which are widely used in 4-class segmentation-based MRAC methods, were used to derive a tissue prior map. The Dixon pulse sequence was developed for separation of fat and water by producing in-phase, out-of-phase, fat and water images from gradient-echo T1-weighted MR images [4]. The fat and water images are segmented into four classes (lung, fat soft-tissue, and outer air) and an additional unknown class indicating regions of low MR intensity corresponding to air cavities, cortical bones and susceptibility artifacts. A co-registered bone map indicating the possible position of bones is also added to the unknown class to include both cortical and spongy bones. Fig. 2 summarizes the procedure. In the proposed method, a mixture of Gaussians (GMM) is used for the estimation of attenuation coefficients over the unknown class of the resulting tissue prior map, while uni-modal Gaussians (constrained GMM) are used over the known tissue classes. In the case of MR truncation artifacts, the outside air, as well as, unknown classes are expanded based on the contour of the estimated TOF activity at the first iteration. The segmentation of non-attenuation corrected TOF activity images has been shown to provide an accurate estimate of external body contour suitable for MR truncation compensation [27]. The MLAA's attenuation corrected TOF activity images can therefore be reliably used for body contour segmentation.

Due to partial volume averaging effect and incomplete fat suppression in the Dixon water images (because of phase errors induced by magnetic field inhomogeneities [28]), spongy bones containing either hematopoietic or fatty tissues can show a moderate MR intensity and therefore might be misclassified as surrounding soft-tissue and fat tissue classes. To eliminate this effect, we heuristically suppressed the fat signal in water images by the subtraction of water and fat images subjected to a non-negativity constraint. As shown in Fig. 3, the spongy bones in the resulting image (e.g. the body and spinous processes of vertebrae) show a zero-intensity and therefore are segmented as belonging to the unknown class. Furthermore, we used a

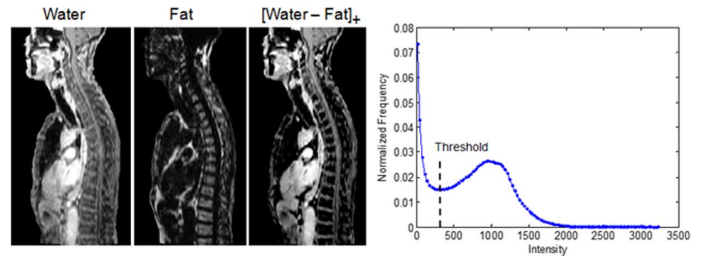


Fig. 3. Soft-tissue segmentation. The fat image is subtracted from the water image (left panel). The resulting image is subjected to a non-negativity constraint and then segmented for soft-tissue at the threshold point corresponding to the local minimum of its histogram (right panel).

TABLE I  
ESTIMATED PARAMETERS OF THE CONSTRAINED GMM OVER  
10 WHOLE-BODY CT IMAGES

MIXTURE OF GAUSSIANS			UNI-MODAL GAUSSIANS		
$\bar{\mu}$	$\sigma$	$\pi$			
0.1205	0.0242	0.5661	LUNG	0.0261	0.0107
0.0980	0.0051	0.2597	FAT	0.0834	0.0013
0.0278	0.0330	0.1150	SOFT	0.0954	0.0012
0.0023	0.0019	0.0592			

bone probability map, obtained from a co-registered average CT, to insure the inclusion of bones into the unknown class. The soft-tissue class was segmented by thresholding the subtraction image at the threshold point corresponding to the local minimum of its histogram (Fig. 3).

The voxels of the fat image whose intensity was 50% larger than the water image were assigned to fat tissue class. The lungs and background air were segmented from in-phase images using a supervised seeded region-growing method implemented in the ITK-SNAP software [29]. Several seeds were manually placed on the regions targeted for segmentation. CT images used to derive the bone map were first converted to a pseudo-MR by setting the intensity of bones to a small value followed by non-rigid registration to the in-phase MR image using the Elastix software [30]. The resulting transformation fields were finally applied to the original CT images. The images were then segmented to extract bones and averaged. A bone map was derived by identifying voxels with a probability larger than 30%. Whole-body CT images of 10 patients (5 females, 5 males, mean age: 68.2 yr, range: 38–79 yr) were used to estimate the parameters of uni-modal Gaussians that best fit the histogram of attenuation coefficients in known tissue classes. For the estimation of the GMM parameters over the unknown class, bones and air gaps were segmented from CT images and the resulting masks were dilated using a morphological operator to mimic the unknown class in tissue prior maps. The distribution of CT attenuation coefficients over the masks were then estimated using a mixture of 4 Gaussians representing inside air, fat/soft mixture and bone using the expectation maximization (EM) algorithm. Table I summarizes the estimated parameters for uni-modal and mixture of Gaussians.

### C. Optimization

The joint MAP in Eq. (2) is not necessarily strictly concave [31], thus the simultaneous estimation of activity and attenuation is not guaranteed to reach a global maximizer. Alternating

optimization, i.e. maximization w.r.t.  $\lambda$  while keeping  $\mu$  constant and vice versa was used to solve Eq. (2) [14]. Similar to the original MLAA algorithm [14], [24], the  $\lambda$  and  $\mu$  optimization steps were solved using ordered subset EM (OSEM) and maximum likelihood for transmission tomography (MLTR) algorithms. Both algorithms are based on optimization transfer, which iteratively defines an easy-to-optimize surrogate for the problem. MLTR uses De Pierro's additive trick and Jensen inequality to surrogate the log-likelihood function [32], [33]. The  $R_{MRF}$  prior is a strictly concave function and can be easily optimized during the  $\mu$  optimization step. Since the  $R_{GMM}$  prior is not concave, we used the Jensen inequality of a log function to define the following surrogate for  $R_{GMM}$  in Eq. (4):

$$\begin{aligned} S_{GMM}(\mu, \mu^n) &= \sum_j \sum_h z_{jh}^n \log \\ &\quad \times \left( \frac{\mathcal{N}(\mu_j | \bar{\mu}_h, \sigma_h)}{\mathcal{N}(\mu_j^n | \bar{\mu}_h, \sigma_h)} \sum_h \pi_h \mathcal{N}(\mu_j^n | \bar{\mu}_h, \sigma_h) \right) \\ &= -\frac{1}{2} \sum_j \sum_h z_{jh}^n \left( \frac{\mu_j^n - \bar{\mu}_h}{\sigma_h} \right)^2 + C \\ z_{jh}^n &= \frac{\pi_h \mathcal{N}(\mu_j^n | \bar{\mu}_h, \sigma_h)}{\sum_q \pi_q \mathcal{N}(\mu_j^n | \bar{\mu}_q, \sigma_q)} \end{aligned} \quad (5)$$

where  $z_{jh}^n$  is obtained from the expectation maximization of GMM and in fact defines the membership probability of  $\mu_j^n$  to class or component  $h$  and  $C$  is a constant value. Note that in a known tissue class  $z_{jh}^n = 1$  and 0 elsewhere; therefore GMM is reduced to a uni-modal Gaussian in that class. As a result, the large deviation of attenuation coefficients from the expected values in each known class is penalized and thus estimations with noise and cross-talk artifacts are effectively suppressed. To this end, the proposed MLAA-GMM algorithm reads as follows

$$\forall i, \quad a_i^n = e^{-\sum_j l_{ij} \mu_j^n} \quad (6)$$

$$\forall j, \quad \lambda_j^{n+1} = \frac{\lambda_j^n}{\sum_i c_{ij} n_i a_i^n} \sum_{it} c_{ijt} n_i a_i^n \frac{g_{it}}{n_i a_i^n \sum_k c_{ikt} \lambda_k^n + n_i \bar{s}_{it} + \bar{r}_{it}} \quad (7)$$

$$\forall i, \quad \psi_i^n = n_i a_i^n \sum_{jt} c_{ijt} \lambda_j^{n+1} \quad (8)$$

$$\forall j; h, \quad z_{jh}^n = \frac{\pi_h \mathcal{N}(\mu_j^n | \bar{\mu}_h, \sigma_h)}{\sum_q \pi_q \mathcal{N}(\mu_j^n | \bar{\mu}_q, \sigma_q)} \quad (9)$$

$$\begin{aligned} \forall j, \quad \mu_j^{n+1} &= \mu_j^n + \alpha \\ &\quad \left( \frac{\sum_i l_{ij} \frac{\psi_i^n}{\psi_i^n + b_i} (\psi_i^n + b_i - g_i) - \gamma \sum_h z_{jh}^n \frac{\mu_j^n - \bar{\mu}_h}{(\sigma_h)^2} - \beta \frac{\partial R_{MRF}(\mu^n)}{\partial \mu_j}}{\sum_i l_{ij} \frac{(\psi_i^n)^2}{\psi_i^n + b_i} \sum_k l_{ik} - \gamma \sum_h \frac{z_{jh}^n}{(\sigma_h)^2} + \beta \frac{\partial^2 R_{MRF}(\mu^n)}{\partial^2 \mu_j}} \right), \end{aligned} \quad (10)$$

where  $b_i = n_i \bar{s}_i + \bar{r}_i$ ,  $c_{ij} = \sum_t c_{ijt}$ ,  $g_i = \sum_t g_{it}$ ,  $\bar{s}_i = \sum_t \bar{s}_{it}$ , and  $\bar{r}_i = \sum_t \bar{r}_{it}$  are TOF-integrated quantities and  $\alpha > 0$  is a step size parameter. Algorithm 1 summarizes the detailed implementation of the proposed method. For both simulation and clinical studies reported in this work, we set  $\alpha = 1.5$ ,  $\beta = 50$ ,  $\gamma = 0.015$ .

---

**Algorithm 1:** MLAA-GMM

---

**Initialize:**  $\mu^0, \lambda^0, \alpha, \beta, \gamma$  and GMM parameters  $\pi, \bar{\mu}, \sigma$  according to Table I.

1. **For** global iterations,  $n = 0, \dots, N$ , **do**
2. Calculate attenuation factors from  $\mu^n$  in Eq. (6).
3. **For** activity sub-iterations, **do**
4. Reconstruct  $\lambda^{n+1}$  using a TOF-OSEM in Eq. (7), initialized by  $\lambda^n$ .
5. **End**
6. **For** attenuation sub-iterations, **do**
7. Calculate the attenuated and normalized non-TOF forward projection of the estimated activity in Eq. (8).
8. Calculate the constrained membership probability of  $\mu^n$  in Eq. (9).
9. Update  $\mu^{n+1}$  using a non-TOF OS-MLTR in Eq. (10).
10. **End**
11. **End**

**Return:**  $\mu^{n+1}, \lambda^{n+1}$

---

#### D. Experiments

We evaluated the performance of the proposed MLAA-GMM algorithm using both simulated and clinical studies in comparison with the original MLAA proposed by Rezaei *et al.* [24] and the MLAA approach proposed by Salomon *et al.* [21]. For simulations studies, phantoms were derived from real clinical studies acquired on PET/CT and PET/MRI scanners installed at our institution.

1) *Clinical PET/CT and PET/MRI Data Acquisition:* PET/CT and MRI datasets of a patient with head and neck carcinoma were acquired on the Biograph mCT flow scanner (Siemens Healthcare) and Ingenuity TF PET/MRI scanner (Philips Healthcare) as part of the clinical workup. The TOF-PET data of the Biograph PET/CT scanner were used for reconstruction of activity and attenuation maps and the anatomical MR images acquired on the Ingenuity PET/MRI scanner were used for the MLAA algorithm. The patients were injected with 280 MBq of  $^{18}\text{F}$ -FDG and underwent a 12 minute PET scan about 60 minutes post-injection with arms-down position. The MR acquisition was performed on the Achieva 3T MRI subsystem of the Ingenuity TF PET/MRI scanner [19]. A whole-body scan was acquired in breath hold mode using a 3D 2-point multi-echo fast field echo Dixon (mDixon) technique using the following parameters: TR = 5.7 ms, TE1/TE2 = 1.45/2.6, flip angle =  $10^\circ$  and slice thickness of 3 mm, matrix size of  $680 \times 680$  and in plane resolution of  $0.67 \text{ mm} \times 0.67 \text{ mm}$ . The acquisition time was limited to about 20 seconds to minimize breath hold time. The Dixon MR images were deformably registered to patient's CT images using the Elastix software.

2) *Experimental Phantom Measurements and Simulations:* The NEMA IEC body phantom was scanned on the mCT scanner to evaluate the quantitative performance of the MLAA algorithm with regard to the missing scaling factor [24]. About 100 MBq of  $^{18}\text{F}$ -FDG were injected in the phantom followed by scanning for 30 minutes. In this experiment, a pseudo MR image was obtained from the corresponding CT images, by reducing the intensity of hollow glass spheres and their acrylic holders, and used to derive a tissue prior map and anatomical regions for MLAA-GMM and MLAA-Salomon algorithms, respectively. For MLAA-Salomon, the pseudo MR image was segmented into  $\sim 300$  regions using a hybrid  $k$ -means and Markov random field clustering algorithm by means of the VolView software (Kitware, Inc., Clifton Park, NY), followed

by connected component labeling. Regions with less than 10 voxels were assigned to their nearest populated regions.

Clinical PET/CT/MRI datasets were used to simulate noisy TOF data acquisitions on the mCT scanner. Two realistic head and thorax phantoms were derived from clinical studies to evaluate the performance the MLAA algorithms for different activity distributions, noise levels and body regions. In the head phantom shown in Fig. 4(a), typical biodistribution of  $^{18}\text{F}$ -FDG and  $^{18}\text{F}$ -Choline (FCH), 60 min and 20 min post-injection were simulated, respectively.  $^{18}\text{F}$ -FDG has an enhanced uptake in the brain and a background uptake over soft-tissues while  $^{18}\text{F}$ -Choline (FCH) has an enhanced uptake in malignant tumors, i.e. glioma, salivary glands (parotids) and a negligible uptake in the brain [34]. The thorax phantom shown in Fig. 4(b) was also derived from an  $^{18}\text{F}$ -FDG PET scan, 60 min post-injection. An in-house TOF-PET simulator was developed for the native geometry of the Siemens Biograph mCT system, with an effective timing resolution of 580 ps and a coincidence window width of 4 ns, using MATLAB with SPMD parallel processing (MathWorks Inc., Natick, MA). The 4D TOF sinograms had 400 radial bins, 168 azimuthal angles, 621 planes (in 9 segments with span 11) and 13 time bins of 312 ps width. The attenuation and activity were reconstructed for a single bed. Projection data were attenuated by actual attenuation factors obtained from the forward projection of CT-based (CTAC) attenuation maps. Poisson noise realizations were simulated for 85 M and 40 M counts in the FDG and FCH head phantoms, respectively, and 40 M counts in the thorax phantom. In the simulations, the contribution of scattered and random coincidences was ignored. For the MR-constrained MLAA algorithms, MR images were coregistered to CT images using the Elastix software, with mutual information similarity measure and 5 resolution levels, and then down-sampled to the resolution of attenuation maps. For the proposed MLAA-GMM algorithm, a tissue prior map was derived from MR images and a co-registered bone map. For MLAA-Salomon algorithm, the T1-weighted in-phase MR images were segmented into many regions for each PET bed position using the above mentioned segmentation method.

### III. RESULTS

#### A. Head and Thorax Phantom Simulations

To evaluate the impact of activity distribution on the performance of the algorithms in estimating attenuation coefficients, the numerically simulated FDG and FCH head phantoms, presented in Section II-D-2, were employed. In the FDG and FCH phantoms, 85 M and 40 M Poisson-distributed counts were respectively simulated from the attenuated forward projection of the true activity distributions. In the FDG data simulation case, the maximum number of counts in the TOF and non-TOF sinograms was 21 and 39, respectively, while in the FCH simulation, it was 19 and 35 for TOF and non-TOF sinograms, respectively. The activity/attenuation pair images were reconstructed with a matrix size of  $400 \times 400 \times 109$  per bed using 40 global iterations, 1 iteration and 2 subsets for activity updates followed by 1 iteration and 3 subsets for attenuation updates.

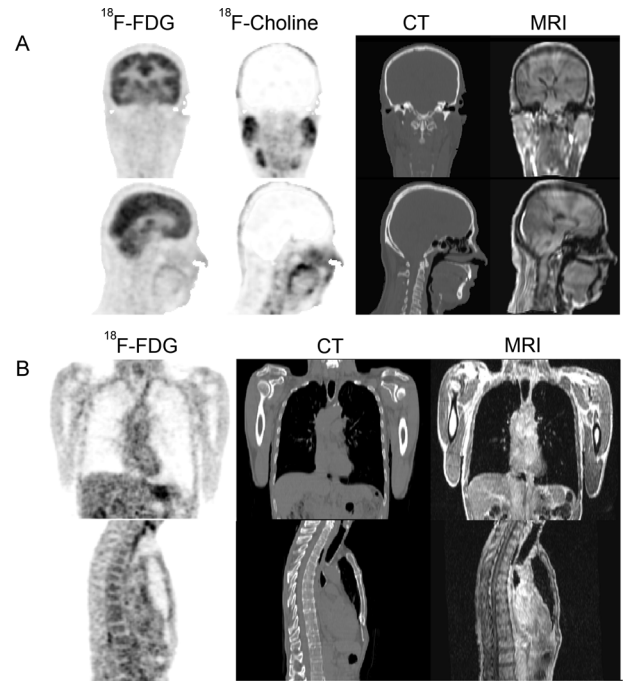


Fig. 4. (a) The head PET/CT/MRI phantom emulating the biodistribution of  $^{18}\text{F}$ -FDG and  $^{18}\text{F}$ -Choline derived from real clinical studies. (b) PET/CT/MRI thorax phantom simulated from an  $^{18}\text{F}$ -FDG clinical study.

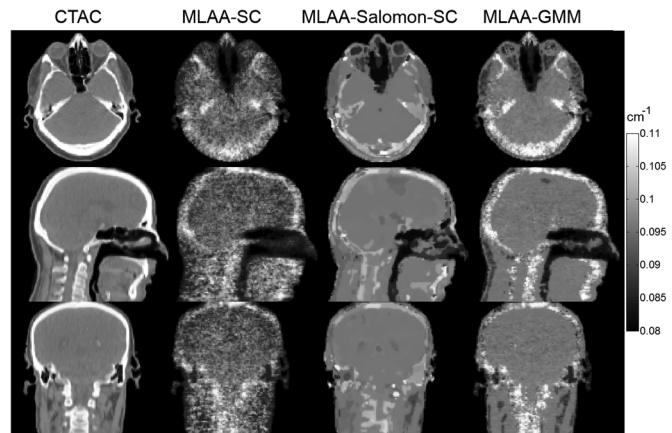


Fig. 5. The estimated attenuation maps using the different MLAA algorithms for the  $^{18}\text{F}$ -FDG head phantom compared with the corresponding reference CTAC map used as reference.

The MLAA activity and attenuation reconstructions are scaled as reported earlier. To solve the scaling problem, Rezaei *et al.* [24] iteratively imposed the known value of tissue attenuation to the 75th percentile of the LACs within the body contour. In this work, we evaluated MLAA and MLAA-Salomon algorithms with and without the scale correction (SC) factor proposed in [24], and the scale correction using the known CTAC PET activity (SC\*) [36]. In addition, we used the same MRF smoothing prior for the MLAA algorithm as for the proposed algorithm. For the studied algorithms, a background mask was imposed on the attenuation maps to set to zero the image voxels outside of CT support.

Fig. 5 compares the estimated attenuation maps of the FDG phantom for the proposed MLAA-GMM and the scale corrected

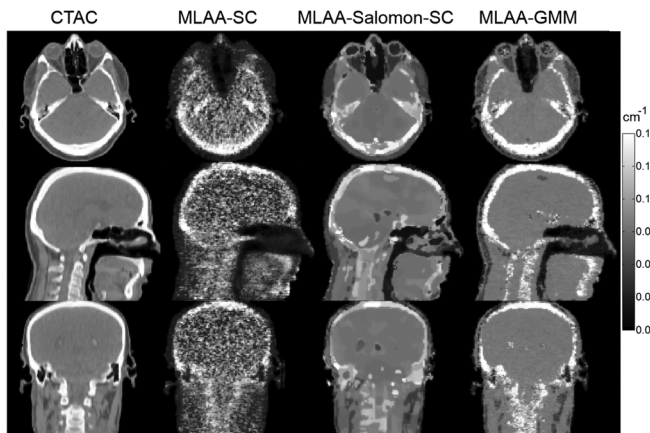


Fig. 6. Same as Fig. 5 for the  $^{18}\text{F}$ -Choline head phantom.

versions of MLAA and MLAA-Salomon algorithms. The results show that the MLAA-SC algorithm distinguishes well air gaps from soft-tissue; however, the estimated attenuation map suffers from noise, especially at the edge of the axial field-of-view, where the sensitivity and thus the support of activity is lower. The MLAA-Salomon-SC algorithm effectively suppresses noise; however, since MR images acquired using conventional MR sequences cannot distinguish bone from air gaps, it cannot accurately differentiate the paranasal and petrous air cavities (see sagittal and coronal slices). For this algorithm, in-phase MR images were segmented into about 4500 distinct regions. Furthermore, because of the region-wise update, the estimated attenuation coefficients of bones are underestimated, indicating the slower convergence of this algorithm. In contrast, the MLAA-GMM algorithm outperforms its counterparts by effective noise suppression, air cavity differentiation and bone derivation. However, the algorithm cannot highlight all bony structures, e.g. temporal and parietal bones in the transverse and coronal slices, respectively, which should be ascribed to count level, convergence rate and activity distribution. Fig. 6 shows the estimated attenuation map of the FCH head phantom where the corresponding PET images have a more asymmetric distribution than the FDG head phantom (Fig. 4) and provide less support for attenuation estimation, given the lower number of simulated counts. As can be seen, the MLAA-SC results in overwhelmingly noisy estimates, while both Salomon's and our algorithm suppress noise effectively. Because of the axially asymmetric distribution of activity or the high uptake of scalp, the algorithm estimates the bones more completely and accurately compared to the FDG phantom. Overall, the proposed MLAA algorithm shows an improved performance over its counterparts in the derivation of the attenuation map. Fig. 7 compares the mean and standard deviation of the estimated attenuation maps for the FDG and FCH head phantoms with the reference CTAC maps for soft and bone tissue classes, respectively.

The linear attenuation coefficients (LACs) estimated by MLAA show a high standard deviation, which is considerably reduced when using MLAA-Salomon and MLAA-GMM algorithms. In soft-tissue, MLAA-GMM estimates the same attenuation coefficients for both phantoms, while the performance of the other algorithms depends on the activity distribution.

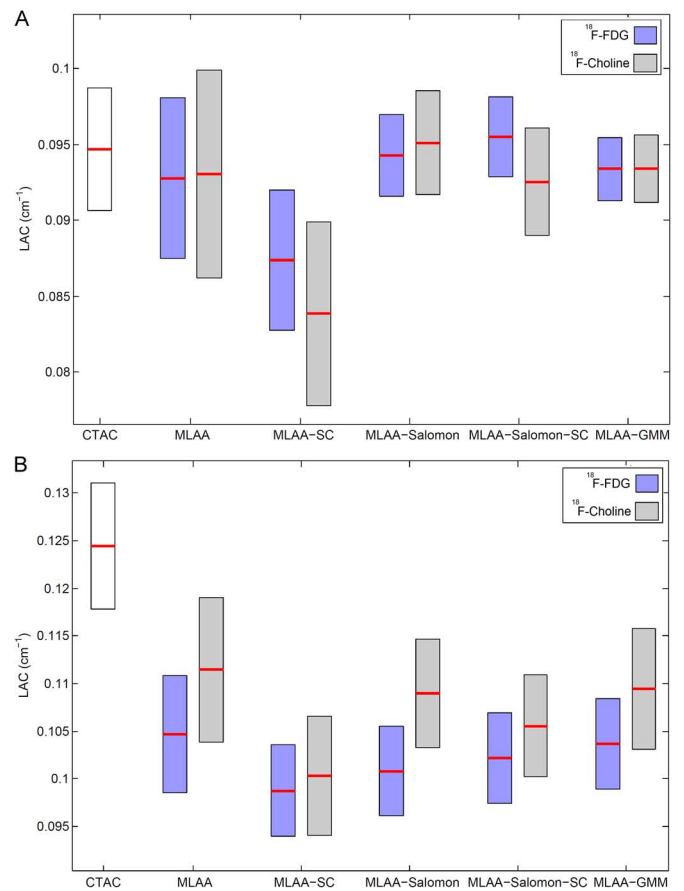


Fig. 7. Comparison between the estimated attenuation maps using the different MLAA algorithms and the reference CTAC map in (a) soft tissue and (b) bone tissue classes for  $^{18}\text{F}$ -FDG and  $^{18}\text{F}$ -Choline head phantoms. The horizontal bars and vertical boxes indicate the mean and standard deviation ( $1\sigma$ ) of attenuation coefficients.

The results show that the scale correction of the MLAA and Salomon's algorithms underestimate the attenuation coefficients, underlining the non-robustness of the scale correction approach proposed in [24].

In bony structures, the algorithms present almost the same quantitative performance and underestimate the mean bone attenuation coefficients; however, as shown in Fig. 6, they can better estimate the bone LACs in the FCH phantom. The quantitative performance of the algorithms was further evaluated with respect to PET images reconstructed using CTAC attenuation maps. Table II summarizes the PET quantification bias of the algorithm for the FDG and FCH studies in three different ROIs (cerebrum, frontal lobe of brain and 4th cervical vertebra, C4).

The results show that the algorithms present with similar performance, which is dependent on the activity distribution. However, the results also show that the scale corrected version of the MLAA and MLAA-Salomon algorithms results in very high bias.

Fig. 8 compares the reconstructed attenuation maps of the thorax phantom with the CTAC attenuation map over 2 overlapping bed positions with 40 M counts per bed. In this simulation, the maximum number of counts in the TOF and non-TOF sinograms was 13 and 26, respectively. The images were reconstructed with the same resolution and number of iterations

TABLE II  
PET QUANTIFICATION BIAS (IN PERCENT) IN DIFFERENT ROIS  
WITH RESPECT TO REFERENCE CTAC-PET IMAGES

	ALGORITHM	CEREBRUM	FRONTAL	C4
FDG	MLAA	$-7.3 \pm 2.7$	$-7.7 \pm 3.2$	$-4.1 \pm 7.7$
	MLAA-SC	$-15.7 \pm 2.4$	$-15.7 \pm 2.8$	$-11.4 \pm 5.6$
	MLAA-SALOMON	$-7.7 \pm 1.4$	$-7.4 \pm 1.8$	$-7.4 \pm 6.5$
	MLAA-SALOMON-SC	$-5.6 \pm 1.5$	$-5.4 \pm 1.8$	$-6.2 \pm 6.5$
	MLAA-GMM	$-7.3 \pm 1.1$	$-7.0 \pm 1.5$	$-6.4 \pm 4.5$
FCH	MLAA	$-0.4 \pm 6.5$	$-1.0 \pm 6.0$	$-3.4 \pm 10.4$
	MLAA-SC	$31 \pm 37.5$	$20.5 \pm 34.0$	$54.2 \pm 55.2$
	MLAA-SALOMON	$-0.3 \pm 1.1$	$-0.3 \pm 1.1$	$-6.4 \pm 7.6$
	MLAA-SALOMON-SC	$41.2 \pm 42.9$	$28.9 \pm 39.7$	$68.0 \pm 63.4$
	MLAA-GMM	$-2.5 \pm 1.1$	$-1.6 \pm 1.2$	$-6.2 \pm 7.3$

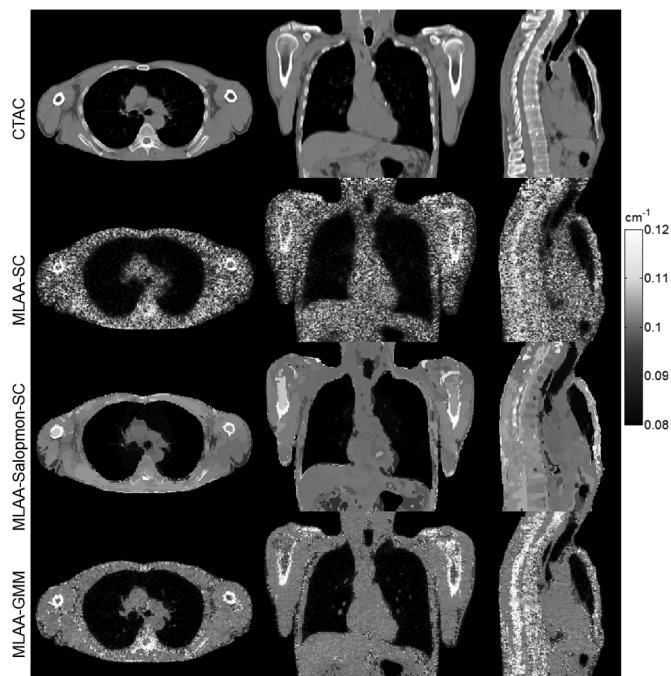


Fig. 8. The estimated attenuation maps using the various MLAA algorithms in the  $^{18}\text{F}$ -FDG thorax phantom compared with their corresponding reference CTAC-based attenuation map.

as the head phantom. For Salomon's algorithm, in-phase MR images corresponding to each bed were segmented into about 5000 distinct regions. As can be seen, MLAA differentiates well the lungs and air pockets; however, the estimated attenuation map suffers from noise. MLAA-Salomon-SC substantially reduces noise by region-wise averaging of the correction matrix (descent direction) during the estimation of attenuation; however, this algorithm is not able to estimate accurately bone attenuation, mainly because of the misclassification of bones with surrounding soft-tissues owing to i) the inherent partial volume averaging effect in the original MR images and the averaging effect induced during down-sampling to  $400 \times 400$  resolution of the mCT images, ii) MR field inhomogeneities, and iii) the limitations of the segmentation algorithm. In contrast, the proposed algorithm outperforms its counterparts in reducing noise and potential cross-talk artifacts and in deriving bony structures.

Fig. 9 shows the mean and standard deviation of the estimated LACs at each global iteration for soft-tissue, lung and bone classes of the thorax phantom. The mean and two-sigma deviation of the true attenuation coefficients are shown by the

horizontal solid lines and yellow bars, respectively. Salomon's algorithm overestimates soft-tissue class, mainly because of the scaling problem of the joint estimation of activity and attenuation. MLAA-Salomon-SC algorithm estimates reasonably well the soft-tissue class, while MLAA-SC algorithm underestimates the mean soft-tissue attenuation coefficients because of inaccurate scale correction. However, the proposed algorithm correctly estimates the mean values with an acceptable standard deviation. In the lungs, as the number of iterations increases, the bias in the mean of estimated lung LACs decreases. Both Salomon and our approach outperform the MLAA algorithm. The algorithms show a monotonic convergence toward the expected value of lung LACs. However, they have not converged and reached a plateau after 40 global iterations, which results in 80 and 120 updates for activity and attenuation maps, respectively. The algorithms have almost the same convergence in the estimation of mean attenuation coefficients of bone, but the proposed algorithm tends to estimate more accurately the mean of bone LACs at earlier iterations, although at later iterations, it approaches the other algorithms.

### B. Experimental NEMA Phantom

In this experiment, the NEMA phantom was located at the center of the field-of-view of the mCT scanner and scanned for 15 minutes using step and go mode. A total number of about 200 M and 100 M prompt and accidental coincidences were recorded in the resulting TOF sinograms. In this phantom, the activity and attenuation maps were reconstructed with a matrix size of  $200 \times 200 \times 109$  for 20 global iterations and the same update schedule as in the simulations. An initial attenuation map was derived by filling the body contour with water attenuation coefficient ( $0.0957 \text{ cm}^{-1}$ ). The CTAC attenuation map was used to enforce bed attenuation values as well as to estimate TOF scatter sinograms using Siemens e7 tools.

Fig. 10 shows the activity and CTAC attenuation maps together with the attenuation maps estimated using MLAA-SC, MLAA-Salomon-SC and MLAA-GMM techniques. The algorithms differentiate well the body attenuating materials from the central cavity of the phantom, which contains lung equivalent density. The MLAA's attenuation map; however, suffers from noise and over-estimation of attenuation coefficients on the top of the phantom, which has an imperfect support of activity. Salomon's algorithm effectively reduces noise, since it updates the attenuation maps on a region-wise basis, while the MLAA-SC and MLAA-GMM algorithms update them on a pixel-wise basis. The region-wise update is efficient provided that an accurate segmentation can be achieved. For this reason, the MLAA-Salomon-SC algorithm performs well over the body of the phantom; however, on the top of the phantom and the 28-mm sphere, it overestimates the attenuation coefficients. The proposed algorithm reduces noise and overestimation by penalizing the large deviation of attenuation coefficients from their expected values.

Fig. 11 compares the activity profiles of the estimated activity maps using the different MLAA-algorithms with the reference CTAC activity profiles. The results show that the MLAA-GMM, MLAA and MLAA-Salomon algorithms have almost the same performance since the scaling issue is not raised in this phantom

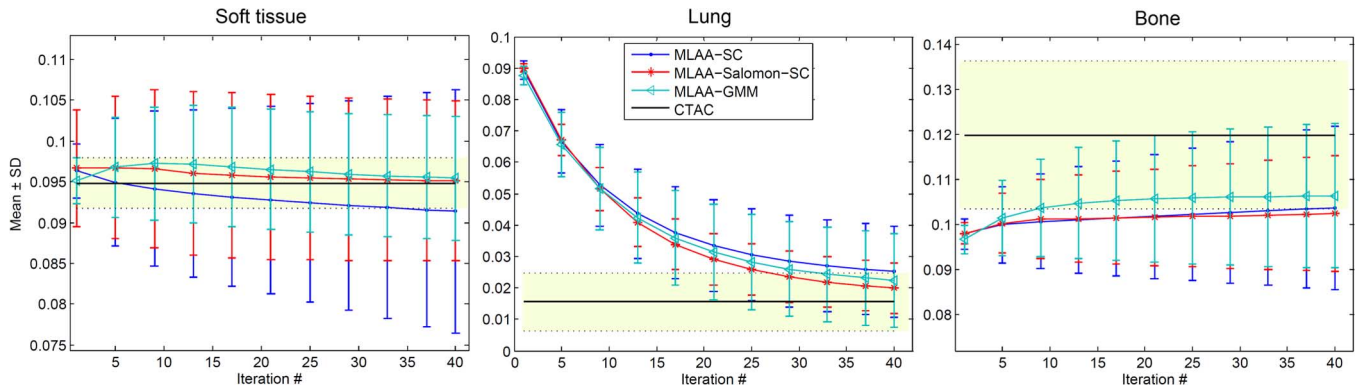


Fig. 9. The mean  $\pm$  standard deviation of the estimated attenuation coefficients vs. the global iteration number in soft-tissue, lung and bone tissue classes of the thorax phantom using 40 M counts simulations. The horizontal solid lines and yellow bars indicate the expected value and the  $2\sigma$  variation of LACs in the reference CTAC map.

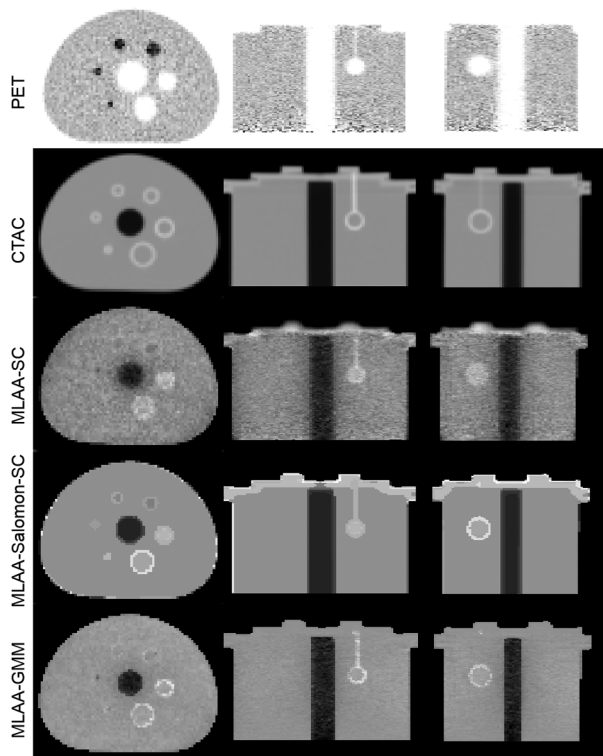


Fig. 10. The NEMA PET activity and corresponding CT-based attenuation map together with the attenuation maps estimated using the various MLAA algorithms with the scale correction (SC) proposed in [24].

study. Consequently, the scale correction of the two latter algorithms results in underestimation of the hot spots activity values. The quantitative performance of the algorithms was further evaluated. In this experimental and the following clinical studies, the mean ( $m^h$ ) and standard deviation ( $\sigma^h$ ) of the activity quantification errors (bias) was evaluated in each tissue class ( $h$ ) as follows:

$$m^h = \frac{\sum_{i \in h} B_i}{N_h}, \quad \sigma^h = \sqrt{\frac{\sum_{i \in h} (B_i - m^h)^2}{N_h}}, \quad B_i = \frac{\lambda_i - \lambda_i^{CT}}{\lambda_i^{CT}} \quad (11)$$

where  $N_h$  is the number of voxels in class  $h$ . In the NEMA phantom, a soft tissue class was derived from the reconstructed

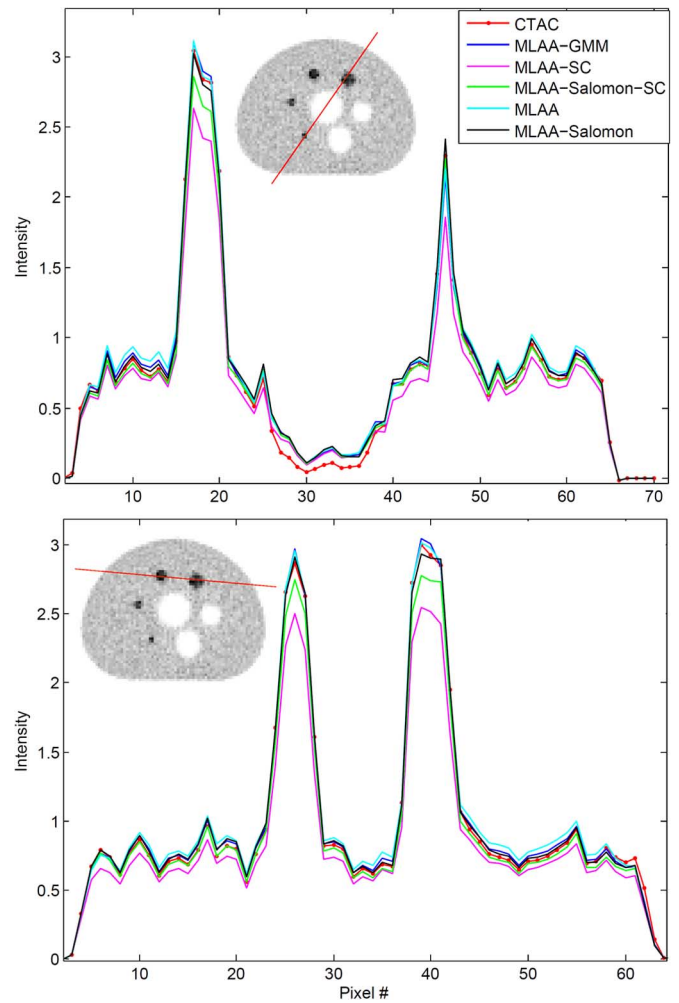


Fig. 11. Activity profiles of the NEMA phantom reconstructed using the studied MLAA algorithms compared with reference CTAC-OSEM.

CTAC PET images, while for the clinical studies, the classes of the tissue prior map were used for bias evaluation. The results show that the MLAA-GMM algorithm gives rise to  $-0.4 \pm 3.2\%$  bias, while the MLAA and MLAA-Salomon result in a bias of  $-3.1 \pm 5.2\%$  and  $-3.1 \pm 4.7\%$ , respectively. The scale corrected version of the algorithms, i.e. MLAA-SC

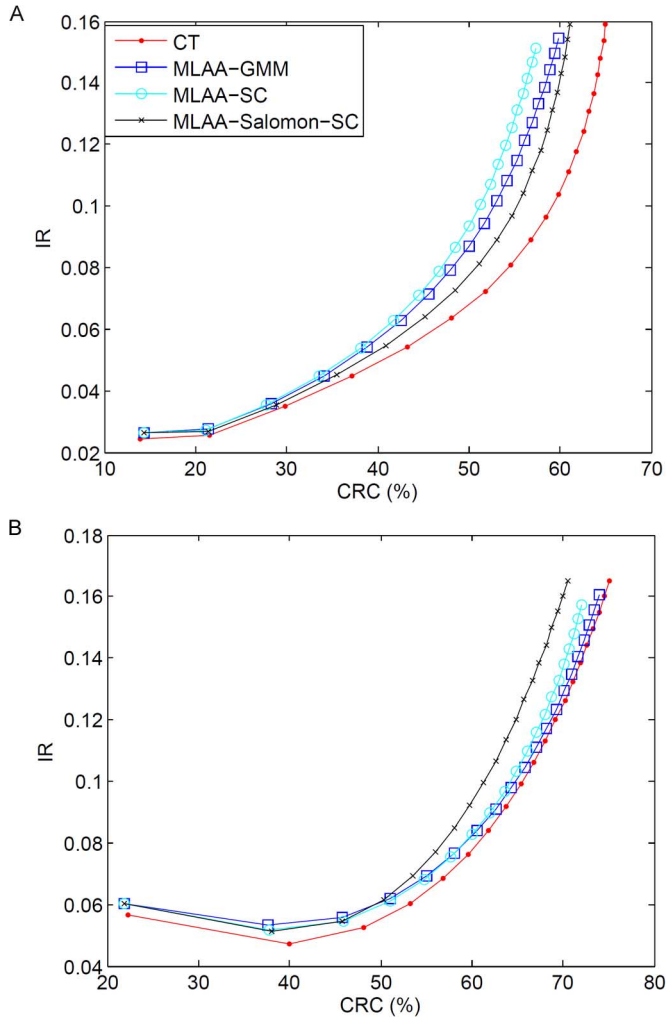


Fig. 12. Image roughness (IR) versus contrast recovery coefficient (CRC) as a function of iteration number for different reconstructions of the NEMA phantom, weighted for (a) all of hot spheres and (b) all of cold spheres according to the size of spheres.

and MLAA-Salomon-SC, resulted in a bias of  $-8.4 \pm 6.2\%$  and  $-0.9 \pm 3.6\%$ , respectively. These results show that the heuristic scale correction method proposed by Rezaei *et al.*, improves the overall quantitative performance of the Salomon's algorithm, while it adversely affects the original MLAA algorithm. The NEMA phantom was further used to evaluate the bias-variance performance of the algorithms in terms of contrast recovery coefficient (CRC) as a metric of bias and image roughness (IR) as a metric of variance, according to the International Atomic Energy Agency (IAEA) protocol [35]. In order to assess the overall quantitative performance, we averaged the IR and CRC values of the hot spheres as well as the cold spheres, based on the size of the spheres (number of voxels in ROIs corresponding to each sphere). Fig. 12 shows the results for hot and cold spheres. For the same noise level in the hot spheres, the MLAA algorithm results in a lower CRC than the reference CTAC-OSEM algorithm. The MLAA-Salomon-SC and MLAA-GMM achieve a slightly better bias-variance performance than MLAA-SC. On the other hand, in the cold spheres, MLAA-Salomon-SC achieves the worst bias-variance trade-off, probably because of an inappropriate scale correction

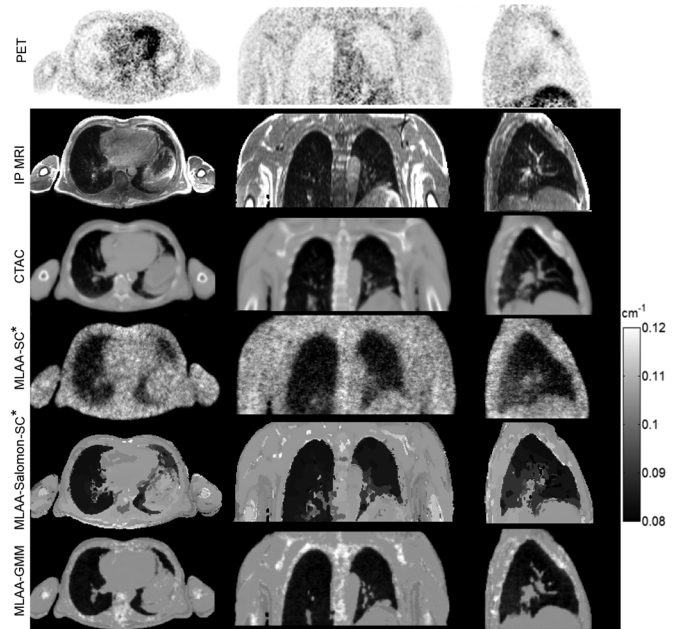


Fig. 13. Comparison of the estimated attenuation maps derived using the different algorithms with the reference CT-based attenuation map for the  $^{18}\text{F}$ -FDG clinical study. The corresponding PET and MR images are also shown.

over the cold spot, where cross-talk artifacts can occur (see Fig. 10 middle column).

### C. Clinical Study and Quantitative Evaluation

A patient presenting with head and neck cancer, injected with 280 MBq  $^{18}\text{F}$ -FDG, underwent a 12 min PET scan on the mCT Flow scanner using continuous bed motion mode. Dixon MR images were acquired on the Ingenuity TF PET/MRI scanner as described in Section II-D-1. PET data of an axial length of about 22 cm corresponding to a single bed position were used for joint reconstruction. The total number of prompts and net trues were about 47 and 30 M counts, respectively.

The MLAA algorithms were initialized with water-equivalent attenuation map and CTAC-simulated scatter. The activity and attenuation maps were reconstructed with a matrix size of  $400 \times 400 \times 109$  using 35 global iterations and the same update schedule as in the simulations. In our simulation and NEMA results, the applied scale correction was not robust, therefore for this dataset, as in [36], we assumed that the total amount of activity is known from the reference CTAC PET image and the activity reconstructions were scaled during reconstructions. We refer to this scale correction as SC\*.

Fig. 13 compares the reconstructed attenuation maps with the reference CTAC attenuation map as well as the corresponding in-phase MR image used in MLAA-Salomon-SC\* and MLAA-GMM algorithms. In this comparison, the attenuation maps were smoothed using a 5 mm FWHM 3D Gaussian filter. The results show that the MLAA-SC\* attenuation map suffers from noise. Salomon's algorithm effectively reduces the noise and artifacts; however, it suffers from MR segmentation errors, especially in the backbone area due to MR field inhomogeneities. In contrast, the proposed algorithm estimates more

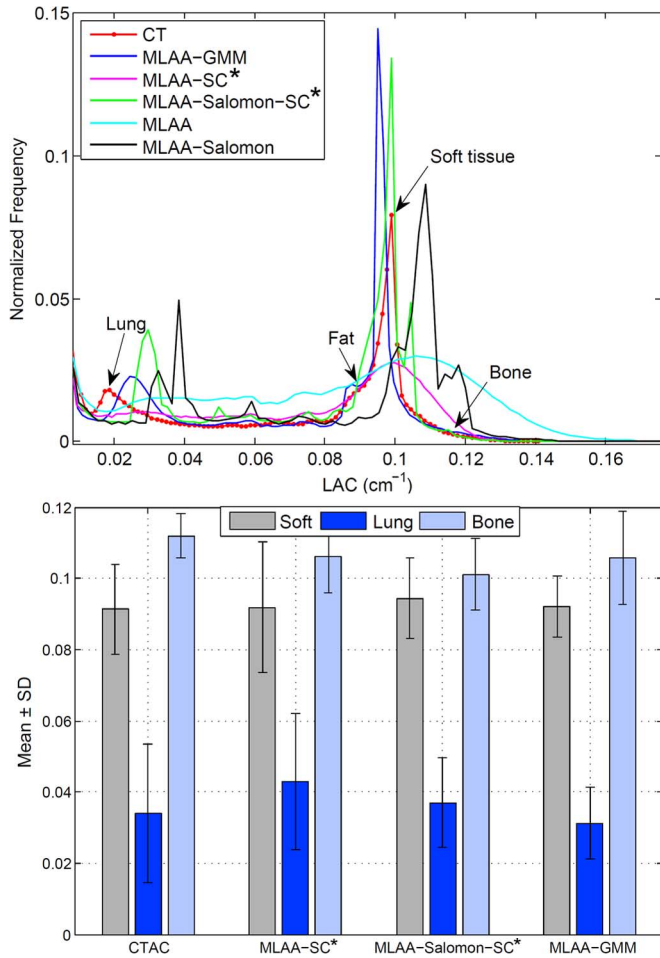


Fig. 14. (a) The normalized histogram of the estimated attenuation maps of the  $^{18}\text{F}$ -FDG clinical study with reference CTAC histograms. (b) The mean  $\pm$  standard deviation of the estimated attenuation coefficients of soft-tissue, lung and bone tissue classes.

accurately the attenuation map through effective suppression of noise, artifacts and the scaling of attenuation.

Fig. 14(a) illustrates the normalized histograms of the reconstructed attenuation maps in comparison with the reference CTAC maps. The peak LACs of the lung and soft-tissue have been shifted toward higher values in the attenuation maps estimated by MLAA and MLAA-Salomon algorithms, while the scale correction of the algorithms reduces the LAC scaling. The soft-tissue peak has been underestimated by MLAA-GMM, mainly because of the high value of the  $\gamma$  parameter of the GMM for this patient dataset. Fig. 14(b) shows the mean  $\pm$  standard deviation of attenuation coefficients in soft-, lung and bone tissue classes obtained from segmentation of the CTAC map. The mean of CTAC and estimated LACs using MLAA-SC\*, MLAA-Salomon-SC\* and MLAA-GMM were 0.095, 0.094, 0.096, 0.095  $\text{cm}^{-1}$  in soft tissues, 0.034, 0.04, 0.037 and 0.031  $\text{cm}^{-1}$  in the lungs and, 0.112, 0.106, 0.101 and 0.106  $\text{cm}^{-1}$  in bones, respectively. Fig. 15 compares the profiles of the estimated activity maps in this patient with respect to reference CTAC activity map along the depicted lines. As can be seen, the activity profiles of the MLAA and MLAA-Salomon algorithms are scaled and overestimate the hot and background

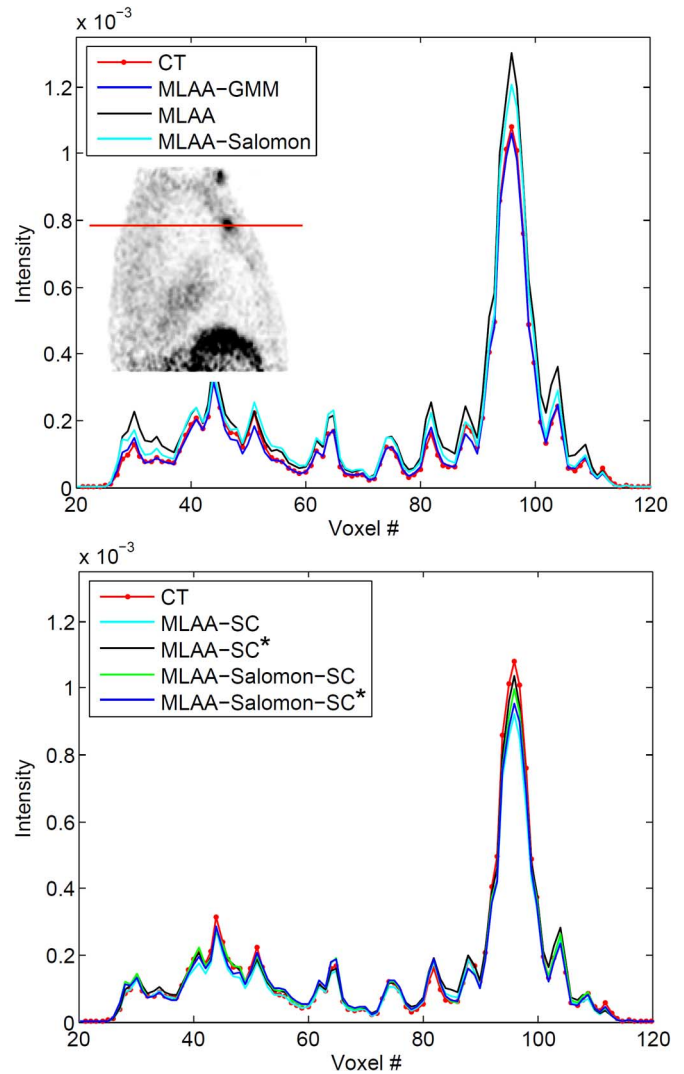


Fig. 15. The activity profiles of the MLAA activity maps for the  $^{18}\text{F}$ -FDG clinical study compared to their reference CTAC-OSEM profiles across an active tumor.

regions. The scale correction of these algorithms using Rezaei's method (SC) tends to suppress the overestimation and improves the performance of the algorithms, however, the activity profile of the lesion tends to be underestimated. On the other hand the scale correction using the known tissue activity (SC\*) can more robustly improve the performance of the algorithms. The results also show that the proposed method can reliably solve the scaling problem of the joint activity/attenuation estimation. The bias performance of the algorithms over soft-tissue, lung and bone classes was also evaluated. Table III summarizes the results of the bias in different tissue classes. Contrary to the NEMA phantom study, the results demonstrate that MLAA and MLAA-Salomon suffer from the scaling problem. The scale correction using SC method improves the results, but the bias is still high, while the SC\* method considerably improves the quantitative performance of the algorithms in soft tissues and bones except in the lungs where the amount tracer uptake is lower. In comparison, the results of MLAA-GMM are quite satisfactory and demonstrate the potential outperformance of

TABLE III  
PERCENT ERROR (BIAS) IN THE ESTIMATED ACTIVITY OF THE FDG CLINICAL STUDY IN DIFFERENT TISSUE CLASSES

ALGORITHM	FAT + SOFT TISSUE	LUNGS	BONES
MLAA	51.8 ± 104.1	98.4 ± 148.2	38.4 ± 75.5
MLAA-SC	-10.4 ± 19.0	19.9 ± 38.9	-17.8 ± 15.5
MLAA-SC*	-0.1 ± 25.1	30.3 ± 45.5	-6.5 ± 21.0
MLAA-SALOMON	24.9 ± 32.3	47.3 ± 40.6	8.6 ± 22.7
MLAA-SALOMON-SC	-2.1 ± 21.6	18.2 ± 32.2	-17.4 ± 14.9
MLAA-SALOMON-SC*	0.9 ± 21.6	16.3 ± 35.2	-13.1 ± 19.1
MLAA-GMM	-0.8 ± 20.2	1.97 ± 22.9	-5.5 ± 19.2

SC: Scale Corrected Using the Method Proposed in [24].

SC\*: Scale Corrected Using Known CTAC Activity [36].

the proposed emission-based method over standard segmentation-based MRAC methods. However, any further conclusion necessitates a comparative study over a larger clinical database.

#### D. GMM Weighting Parameter and Respiratory Artifacts

In this section, we further evaluated the impact of the GMM weighting parameter,  $\gamma$ , on the performance of the proposed algorithm, as well as its behavior in the presence of respiratory-phase mismatch between MRI and PET images. A clinical  $^{18}\text{F}$ -FCH PET/CT dataset was used to evaluate the impact of the  $\gamma$  parameter on the reduction of noise, cross-talk artifacts and the dependency on the activity distribution. A single bed scan covering the head was selected for the reconstruction. The sinogram contained a total number of about 80 M and 50 M prompt and accidental coincidences, respectively. The activity and attenuation maps were reconstructed with a matrix size of  $200 \times 200 \times 109$  using 20 global iterations and the same update schedule as in the previous studies. For this dataset, MR images were not available. Therefore the tissue prior map was derived from the CTAC map. Fig. 16(a) compares the reconstructed attenuation maps with increasing values of the  $\gamma$  parameter from zero (corresponding to the original MLAA) to 1. Fig. 16(b) shows the mean  $\pm$  standard deviation of the estimated LACs in soft tissue in comparison with the reference CTAC. The proposed MLAA is in essence between the standard 4-class MRAC method and the original MLAA algorithm, depending on the GMM prior weight. Very low  $\gamma$ s reduce the algorithm to the original MLAA, while high-valued  $\gamma$  ensure a 4-class MRAC method, where the deviation of attenuation coefficients from their expected 4-class values are penalized. The GMM prior effectively reduces noise and cross-talk artifacts (see the cranial area of the attenuation map with  $\gamma = 0$ ). Consequently, the mean of the attenuation coefficients gets close to the expected values. However, the results show that high values of  $\gamma$  do not easily allow the differentiation of air attenuation coefficients in the unknown tissue class from their initial water attenuation coefficients. In cases where the  $\gamma$  parameter is assigned a high value to benefit from the GMM prior and at the same time to avoid parameter optimization, a practical solution for this differentiation would be the gradual increase of the  $\gamma$  with iteration number (i.e. smooth forcing of the prior), where different tissues in the unknown class can be more accurately captured by Gaussian mixture model. In the case of respiratory-phase mismatch between MRI and PET images, the proposed algorithm should fairly compensate for this mismatch. Since patients spend more time in expiration than in inspira-

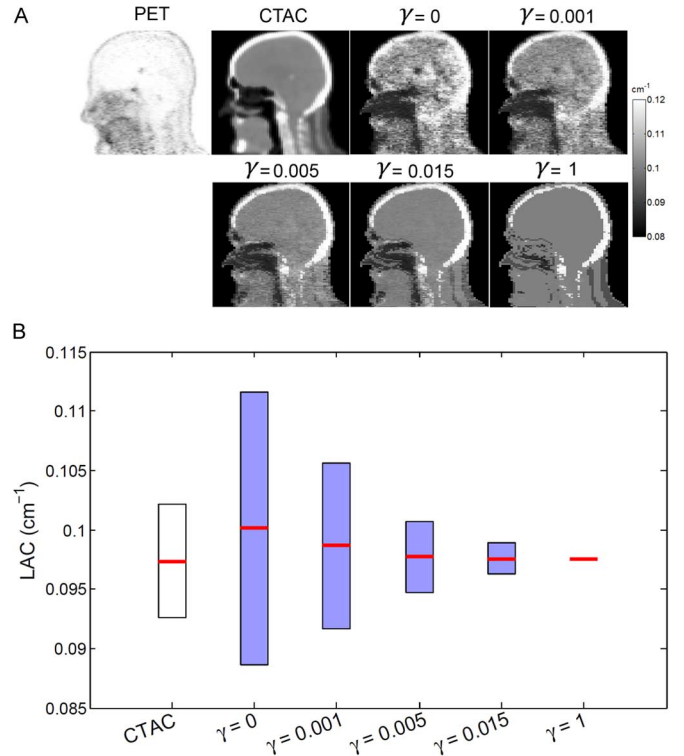


Fig. 16. (a) The impact of the GMM weighting parameter on the performance of the MLAA-GMM algorithm in a clinical  $^{18}\text{F}$ -FCH PET/CT dataset. (b) The estimated attenuation coefficients in soft tissue for the studied weights. The horizontal bars and vertical boxes indicate the mean and standard deviation (1  $\sigma$ ) of attenuation coefficients.

tion during the respiratory cycle, the PET data, averaged over few minutes, are closer to the end of expiration than inspiration [37]. Therefore, if MR images are acquired near end-expiration, MR and PET images should be well aligned. However, if MR images are acquired at for example end-inspiration (severe mismatch), the proposed and original MLAA algorithms should be able to compensate for this mismatch. Fig. 17 compares the CT attenuation map of a clinical study over an axial length of 33 cm with the attenuation map estimated by the proposed algorithm. As the horizontal lines indicate, the two images correspond to the same respiratory phase because, as mentioned in Section II-B, MR images used in the MLAA-GMM algorithm were registered to reference CT images. However, a close examination of non-TOF PET images reveals the presence of respiratory-induced banana artifacts in the diaphragm region depicting a mismatch between PET and CT and thus PET and MR

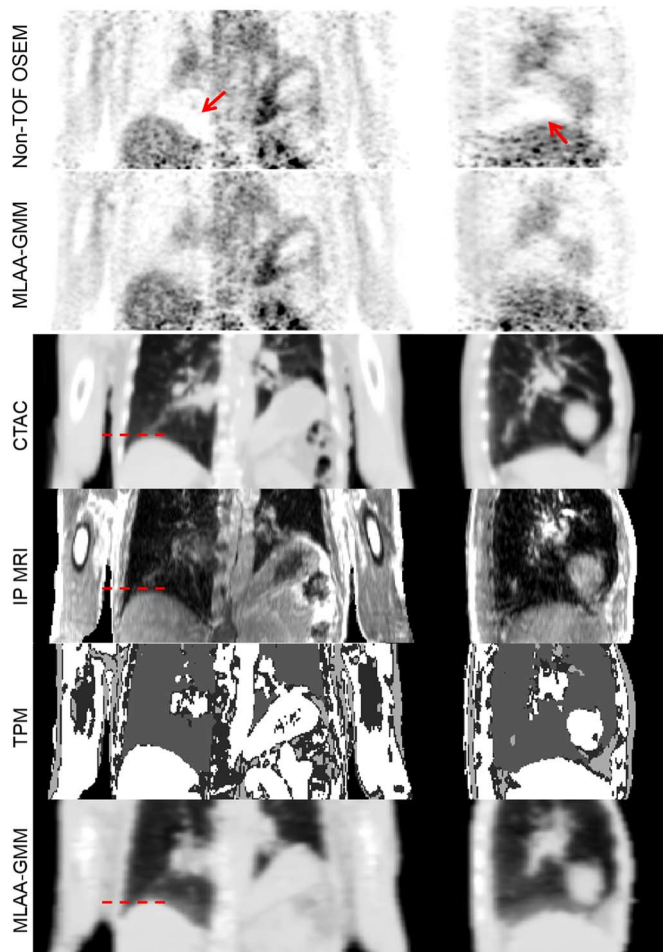


Fig. 17. The non-TOF PET reconstruction of a clinical  $^{18}\text{F}$ -FDG study, showing white-band respiratory artifacts, together with CTAC, IP MRI, tissue prior map (TPM) and MLAA-GMM attenuation map. The horizontal lines demonstrate that both CT and MR images are well co-registered. As pointed by the arrow, there is a respiratory-phase mismatch between PET and CT/MRI images; however, the MLAA-GMM algorithm has compensated for this mismatch. The display window for attenuation maps is  $[0.07\text{--}0.10\text{ cm}^{-1}]$ .

images. The TOF OSEM and MLAA-GMM PET images did not visually reveal the artifacts. Nonetheless, the results demonstrate that the proposed algorithm has well inherited the respiratory mismatch compensation from the original MLAA algorithm (cf. sagittal images) and therefore can reduce the resulting quantification errors.

#### IV. DISCUSSION

Accurate PET attenuation correction in quantitative PET/MRI examinations is of paramount importance. In this work, we proposed a novel approach to effectively employ MRI information in the joint estimation of activity and attenuation from emission data to pave the way toward accurate emission-based attenuation correction in whole-body PET/MR imaging.

Recently introduced commercial PET/MRI systems use standard 3- or 4-class segmentation-based MRAC methods. However, the inter/intra-patient heterogeneity of attenuation coefficients in different tissue classes is ignored by these techniques. Moreover, since bone and air cannot be well dif-

ferentiated on conventional MR sequences, owing to their low water content and short transverse relaxation time, they are often ignored and replaced by soft-tissue, which can lead to significant bias (4 to 25%) in PET tracer uptake quantification in different organs [38]–[41]. Ultra-short echo time (UTE) pulse sequences have been recently explored to include bones as a 5th class in order to reduce the bias [42], [43]. However, despite the promising results, UTE sequences are not yet clinically feasible in whole-body PET/MR imaging owing to long acquisition time. In addition, the images are also subject to misclassifications due to magnetic susceptibility artifacts at air/bone-soft-tissue interfaces [42] and eddy current artifacts [44].

Following the recent rebirth of time-of-flight PET, simultaneous estimation of activity and attenuation has regained popularity for attenuation correction on standalone PET [24] and hybrid PET/MRI systems [21] with spin-off applications in motion and misalignment correction between CTAC attenuation and PET activity maps [45]. The joint estimation is especially attractive for PET/MRI to circumvent the uncertainties and obstacles of the standard and UTE MRAC methods. However, as mentioned earlier, the quantitative accuracy of this estimation using the standard MLAA algorithm depends significantly on TOF timing resolution, count level and activity distribution. The latter supports the estimation of attenuation along LORs that intersect a region containing a substantial amount of activity and in fact determines the degree to which the attention maps can be accurately and completely estimated as demonstrated in our simulated FDG and FCH studies. It has been theoretically and experimentally shown that attenuation maps or attenuation correction factors can be estimated from TOF emission data up to a constant factor. Our experimental phantom and clinical studies showed that the scaling factor of the MLAA algorithm is also object-dependent. Several scenarios have been proposed to practically tackle this scaling issue by rescaling the estimated LACs [24], shifting the peak of the histogram of the estimated attenuation map to soft-tissue attenuation [46], or combining MLAA with full or partial transmission information [47], [48]. The scatter coincidences at a lower energy window [49], single events [50] and background radiation of LSO and LYSO crystals can also provide additional information about the attenuating material and hence a potential solution to this scaling factor [51].

In this work, a Gaussian mixture model was employed in the estimation of attenuation in order to reflect the prior knowledge that the histogram of the attenuation values generally consists of a few distinct peaks corresponding to fat, soft-tissue and bone. The spatial information derived from Dixon MR images is also incorporated into this model to favor known tissue types. A direct result of this spatially constrained tissue preference prior is the penalization of large deviations of attenuation coefficients from their expected value in each known tissue class and their distribution from a histogram parameterized over a patient population. Therefore, as our experimental and clinical results demonstrate, the scaling of attenuation and activity as well as noise and cross-talk artifacts in the attenuation map can be robustly suppressed. In addition, the LACs of regions that are out of the support of activity but are in a known tissue class are recovered more accurately. In comparison, Salomon's algorithm

uses MR images to derive many distinct regions over which attenuation coefficients are estimated without additional information about their expected values.

As spongy bones, containing bone marrow, are usually misclassified as fat and soft-tissue in MR images, we proposed a simple way to suppress fat from water and thus enabling to estimate the voxels of bony structures using a GMM model. Moreover, we employed a co-registered bone probability map, obtained from several co-registered CT images, to indicate regions with possible bone occurrence. Bezrukov *et al.* [38] recently used a bone and metal-artifact probability map to merge 4-class MRAC with an atlas- and pattern recognition-based MRAC algorithm. As mentioned earlier, a perfect atlas-to-patient registration can likely solve the MRAC problem. However, whole-body registration is subject to anatomical differences between subjects and the limitations of registration algorithms. The bone map registration used in our work is, in principle, not subject to such limitations owing to the inherent tolerance conveyed by averaging of CT images. Furthermore, since cortical bones (skull, body of vertebra, hips, etc.) in our heuristically fat suppressed water images are assigned to the low-intensity MR class, the attenuation coefficients of cortical bones are still guaranteed to be estimated with a mixture model in cases of severe mis-registration between MR and bone map. In the presence of MR susceptibility artifacts, MR void regions, which have no intensity, are included in the unknown class and therefore estimated using a GMM model.

Despite the capabilities of the proposed MLAA-GMM algorithm, it is worth to highlight some of its limitations and potential directions for future development to improve its performance. Similar to segmentation-based MRAC methods, the lungs must be segmented as accurately as possible, since the LAC of anatomical structures that are either missed or incorrectly segmented can be wrongly estimated, depending on the user-defined weight,  $\gamma$ , of the GMM prior. Moreover, in the case of mis-registration between MRI and PET images over stomach air pockets, the proposed approach cannot compensate for this mismatch, similar to Salomon's algorithm. In a known tissue class, the objects or structures with an unexpected attenuation coefficient (i.e. misclassified spongy bone or small metallic objects that do not produce MR susceptibility artifacts) can be partially or completely suppressed, depending on the  $\gamma$  parameter.

Similar to other MAP image reconstruction strategies, the performance of the proposed algorithm depends on the choice of the hyper-parameters. In this proof-of-principle study, we tried to fix most of the involved parameters (schedule update, regularization parameters, activity and attenuation initializations) based on our simulation results. As shown in Fig. 16, the performance of the MLAA-GMM depends mainly on the  $\gamma$  parameter. In our experience, this parameter outweighs the  $\beta$  parameter of the MRF prior, therefore there is a flexibility in the selection of  $\beta$ . To avoid optimization of the  $\gamma$  over a large patient dataset, it can be chosen to a high value (based on few simulation or clinical results), which indeed enforces the algorithm toward the underlying 4-class MRAC method. To avoid the tissue differentiation of the unknown LACs with a high-valued  $\gamma$ , the parameter can be gradually increased to the desired value with iteration or update number. Similar to Salomon *et al.*, we initialized the

activity and attenuation with uniform maps and updated them using global and local iterations. In contrast, Rezaei *et al.* used a different update schedule. They performed 3 iterations of 42 subsets for activity update whereas attenuation was updated 3 times after each update of activity for reconstruction of clinical studies. In fact, the MLAA algorithms are still in their infancy and require in-depth exploration of the impact of update schedules and initializations.

In the derivation of bone maps, CT registrations increase the number of preprocessing steps and the overall processing time, although in our experience, the most time consuming part is the TOF joint estimation of activity and attenuation. In brain studies where the skull is mainly cortical and presents with a low MR intensity, we believe that the bone map registration step of the algorithm can be skipped since the bones can be properly included in the unknown tissue class. Moreover, the combination of T1 and proton-density weighted imaging and MR sequences that provide bone-cartilage contrast (i.e. T2-weighted water-excitation dual-echo steady-state and T2-weighted multi-echo data image combination) might provide a solution to better distinguish fat and soft-tissue from spongy bones and thus to eliminate the bone probability map. Future work will focus on the evaluation of the algorithm in brain studies and comparison of its performance with the standard 4-class MRAC method using a large whole-body clinical database through 4-class attenuation initialization and scatter simulation.

## V. CONCLUSION

In this work, an emission-based MRAC algorithm was proposed based on the maximum likelihood reconstruction of activity and attenuation with incorporation of prior MR information using a constrained Gaussian mixture model. The performance of the proposed MLAA-GMM algorithm was evaluated against current state-of-the-art MLAA algorithms using simulation, experimental and clinical studies. The results demonstrate that our algorithm is not susceptible to MR segmentation errors and provides a practical solution to the cross-talk and scaling problems of activity and attenuation estimates, through panelizing large deviations of attenuation coefficients from their expected values in each MR tissue class and overall attenuation distribution from its expected histogram.

## ACKNOWLEDGMENT

The authors would like to thank Michael E. Casey and Judson P. Jones (Siemens Healthcare) for providing and supporting VG50 e7 tools for the CBM mode reconstruction of the mCT Flow scanner.

## REFERENCES

- [1] D. A. Torigian *et al.*, "PET/MR Imaging: Technical aspects and potential clinical applications," *Radiology*, vol. 267, pp. 26–44, 2013.
- [2] I. Bezrukov, F. Mantlik, H. Schmidt, B. Scholkopf, and B. J. Pichler, "MR-based PET attenuation correction for PET/MR imaging," *Sem. Nucl. Med.*, vol. 43, pp. 45–59, 2013.
- [3] H. Zaidi, "Is MRI-guided attenuation correction a viable option for dual-modality PET/MR imaging?," *Radiology*, vol. 244, pp. 639–642, 2007.
- [4] A. Martinez-Moller *et al.*, "Tissue classification as a potential approach for attenuation correction in whole-body PET/MRI: Evaluation with PET/CT data," *J. Nucl. Med.*, vol. 50, pp. 520–526, 2009.

- [5] Z. Hu *et al.*, "MR-based attenuation correction for a whole-body PET/MR system," in *Proc. IEEE Nucl. Sci. Symp. Med. Imag. Conf.*, 2010, pp. 2119–2122.
- [6] M. Hofmann *et al.*, "MRI-based attenuation correction for PET/MRI: A novel approach combining pattern recognition and Atlas registration," *J. Nucl. Med.*, vol. 49, pp. 1875–1883, 2008.
- [7] E. Schreibmann *et al.*, "MR-based attenuation correction for hybrid PET-MR brain imaging systems using deformable image registration," *Med. Phys.*, vol. 37, pp. 2101–2109, 2010.
- [8] A. Johansson, M. Karlsson, and T. Nyholm, "CT substitute derived from MRI sequences with ultrashort echo time," *Med. Phys.*, vol. 38, pp. 2708–2714, 2011.
- [9] B. K. Navalpakkam, H. Braun, T. Kuwert, and H. H. Quick, "Magnetic resonance-based attenuation correction for PET/MR hybrid imaging using continuous valued attenuation maps," *Invest. Radiol.*, vol. 48, pp. 323–332, 2013.
- [10] F. Natterer, "Determination of tissue attenuation in emission tomography of optically dense media," *Inverse Probl.*, vol. 9, pp. 731–736, 1993.
- [11] A. Welch *et al.*, "Attenuation correction in PET using consistency information," *IEEE Trans. Nucl. Sci.*, vol. 45, no. 6, pp. 3134–3141, Dec. 1998.
- [12] A. V. Bronnikov, "Reconstruction of attenuation map using discrete consistency conditions," *IEEE Trans. Med. Imag.*, vol. 19, no. 5, pp. 451–462, May 2000.
- [13] C. H. Wu, J. M. M. Anderson, M. Rao, and B. Mair, "Iterative methods for correcting attenuation in positron emission tomography," in *Proc. Int. Conf. Image Process.*, 1998, pp. 700–705.
- [14] J. Nuyts *et al.*, "Simultaneous maximum a posteriori reconstruction of attenuation and activity distributions from emission sinograms," *IEEE Trans. Med. Imag.*, vol. 18, no. 5, pp. 393–403, May 1999.
- [15] A. Krol *et al.*, "An EM algorithm for estimating SPECT emission and transmission parameters from emissions data only," *IEEE Trans. Med. Imag.*, vol. 20, no. 3, pp. 218–232, Mar. 2001.
- [16] M. Landmann, S. N. Reske, and G. Glatting, "Simultaneous iterative reconstruction of emission and attenuation images in positron emission tomography from emission data only," *Med. Phys.*, vol. 29, pp. 1962–1967, 2002.
- [17] M. S. Kaplan, D. R. Haynor, and H. Vija, "A differential attenuation method for simultaneous estimation of SPECT activity and attenuation distributions," *IEEE Trans. Nucl. Sci.*, vol. 46, no. 3, pp. 535–541, Jun. 1999.
- [18] F. Crepaldi and A. R. De Pierro, "Activity and attenuation reconstruction for positron emission tomography using emission data only via Maximum Likelihood and iterative data refinement," *IEEE Trans. Nucl. Sci.*, vol. 54, no. 1, pp. 100–106, Feb. 2007.
- [19] H. Zaidi *et al.*, "Design and performance evaluation of a whole-body Ingenuity TF PET-MRI system," *Phys. Med. Biol.*, vol. 56, pp. 3091–3106, 2011.
- [20] A. Salomon, A. Goedicke, and T. Aach, "Simultaneous reconstruction of activity and attenuation in multi-modal ToF-PET," in *Proc. 10th Int. Meet. Fully Three-Dimensional Image Reconstruct. Radiol. Nucl. Med.*, Beijing, China, Sep. 5–10, 2009, pp. 339–342.
- [21] A. Salomon, A. Goedicke, B. Schweizer, T. Aach, and V. Schulz, "Simultaneous reconstruction of activity and attenuation for PET/MR," *IEEE Trans. Med. Imag.*, vol. 30, no. 3, pp. 804–813, Mar. 2011.
- [22] T. G. Turkington and J. M. Wilson, "Attenuation artifacts and time-of-flight PET," in *IEEE Nucl. Sci. Symp. Conf. Rec.*, 2009, pp. 2997–2999.
- [23] M. Conti, "Why is TOF PET reconstruction a more robust method in the presence of inconsistent data?," *Phys. Med. Biol.*, vol. 56, pp. 155–168, 2011.
- [24] A. Rezaei *et al.*, "Simultaneous reconstruction of activity and attenuation in time-of-flight PET," *IEEE Trans. Med. Imag.*, vol. 31, no. 12, pp. 2224–2233, Dec. 2012.
- [25] M. Defrise, A. Rezaei, and J. Nuyts, "Time-of-flight PET data determine the attenuation sinogram up to a constant," *Phys. Med. Biol.*, vol. 57, pp. 885–899, 2012.
- [26] J. M. M. Anderson, K. Yoon-Chul, and J. T. Votaw, "Concurrent segmentation and estimation of transmission images for attenuation correction in positron emission tomography," *IEEE Trans. Nucl. Sci.*, vol. 56, no. 1, pp. 136–146, Feb. 2009.
- [27] S. D. Wollenweber *et al.*, "Comparison of 4-class and continuous fat/water methods for whole-body, MR-based PET attenuation correction," *IEEE Trans. Nucl. Sci.*, vol. 60, no. 5, pp. 3391–3398, Oct. 2013.
- [28] J. Ma, "Dixon techniques for water and fat imaging," *J. Magn. Reson. Imag.*, vol. 28, pp. 543–558, 2008.
- [29] P. A. Yushkevich *et al.*, "User-guided 3D active contour segmentation of anatomical structures: Significantly improved efficiency and reliability," *Neuroimage*, vol. 31, pp. 1116–1128, 2006.
- [30] S. Klein, M. Staring, K. Murphy, M. A. Viergever, and J. P. W. Pluim, "elastix: A toolbox for intensity-based medical image registration," *IEEE Trans. Med. Imag.*, vol. 29, no. 1, pp. 196–205, Jan. 2010.
- [31] N. H. Clinthorne, J. A. Fessler, G. D. Hutchins, and W. L. Rogers, "Joint maximum likelihood estimation of emission and attenuation densities in PET," in *Conf. Rec. IEEE Nucl. Sci. Symp. Med. Imag. Conf.*, 1991, pp. 1927–1932.
- [32] J. Nuyts *et al.*, "Iterative reconstruction for helical CT: A simulation study," *Phys. Med. Biol.*, vol. 43, pp. 729–737, 1998.
- [33] J. A. Fessler, E. P. Ficaro, N. H. Clinthorne, and K. Lange, "Grouped-coordinate ascent algorithms for penalized-likelihood transmission image reconstruction," *IEEE Trans. Med. Imag.*, vol. 16, no. 2, pp. 166–175, Apr. 1997.
- [34] O. Schillaci *et al.*, "18F-choline PET/CT physiological distribution and pitfalls in image interpretation: Experience in 80 patients with prostate cancer," *Nucl. Med. Commun.*, vol. 31, pp. 39–45, 2010.
- [35] "Quality assurance for PET and PET/CT systems," IAEA Human Health Series I 2009.
- [36] A. Rezaei, M. Defrise, and J. Nuyts, "ML-reconstruction for TOF-PET with simultaneous estimation of the attenuation factors," *IEEE Trans. Med. Imag.*, vol. 33, pp. 1563–1572, 2014.
- [37] T. Pan and H. Zaidi, "Attenuation correction strategies for positron emission tomography/computed tomography and 4-Dimensional positron emission tomography/computed tomography," *PET Clin.*, vol. 8, pp. 37–50, 2013.
- [38] I. Bezrukov *et al.*, "MR-based attenuation correction methods for improved PET quantification in lesions within bone and susceptibility artifact regions," *J. Nucl. Med.*, vol. 54, pp. 1768–1774, 2013.
- [39] J. Ouyang, S. Y. Chun, Y. Petibon, A. A. Bonab, N. Alpert, and G. El Fakhri, "Bias atlases for segmentation-based PET attenuation correction using PET-CT and MR," *IEEE Trans. Nucl. Sci.*, vol. 60, pp. 3373–3382, 2013.
- [40] D. Izquierdo-Garcia *et al.*, "Comparison of MR-based attenuation correction and CT-based attenuation correction of whole-body PET/MR imaging," *Eur. J. Nucl. Med. Mol. Imag.*, vol. 41, pp. 1574–1584, 2014.
- [41] H. Arabi *et al.*, "Clinical assessment of MR-guided 3-class and 4-class attenuation correction in PET/MR," *Mol. Imag. Biol.*, to be published.
- [42] V. Keereman *et al.*, "MRI-based attenuation correction for PET/MRI using ultrashort echo time sequences," *J. Nucl. Med.*, vol. 51, pp. 812–818, 2010.
- [43] Y. Berker *et al.*, "MRI-based attenuation correction for hybrid PET/MRI systems: A 4-class tissue segmentation technique using a combined Ultrashort-Echo-Time/Dixon MRI sequence," *J. Nucl. Med.*, vol. 53, pp. 796–804, 2012.
- [44] A. P. Aitken *et al.*, "Improved UTE-based attenuation correction for cranial PET-MR using dynamic magnetic field monitoring," *Med. Phys.*, vol. 41, p. 012302, 2014.
- [45] A. Rezaei and J. Nuyts, "Simultaneous reconstruction of the activity image and registration of the CT image in TOF-PET," in *IEEE Nucl. Sci. Symp. Med. Imag. Conf.*, 2013, pp. 1–3.
- [46] R. Boellaard, M. B. Hofman, O. S. Hoekstra, and A. A. Lammertsma, "Accurate PET/MR quantification using time of flight MLAA image reconstruction," *Mol. Imag. Biol.*, vol. 16, pp. 469–477, 2014.
- [47] V. Y. Panin, M. Aykac, and M. E. Casey, "Simultaneous reconstruction of emission activity and attenuation coefficient distribution from TOF data, acquired with external transmission source," *Phys. Med. Biol.*, vol. 58, pp. 3649–3669, 2013.
- [48] C. C. Watson, "Supplemental transmission method for improved PET attenuation correction on an integrated MR/PET," *Nucl. Instrum. Meth. A*, vol. 734, pt. B, pp. 191–195, 2014.
- [49] Y. Berker, F. Kiessling, and V. Schulz, "Use of scattered coincidences for emission-based estimation of attenuation map in PET," in *IEEE Nucl. Sci. Symp. Med. Imag. Conf.*, 2012, pp. 2285–2287.
- [50] C. M. Laymon and T. G. Turkington, "Calculation of attenuation factors from combined singles and coincidence emission projections," *IEEE Trans. Med. Imag.*, vol. 18, pp. 1194–1200, 1999.
- [51] H. Rothfuss *et al.*, "LSO background radiation as a transmission source using time of flight," *Phys. Med. Biol.*, vol. 59, pp. 5483–5500, 2014.